Nano Research

Open Access

Research Article

A self-powered triboelectric nano-sensor enabled digital twin for self-sustained machine monitoring in smart mine

Jianping Jiang[1,4], Chengliang Fan[3], Hongyu Chen[5], Fan Wu[1,4], Xihui Feng[3], Canjun Xiao[2], Hongye Pan[1,4], Xiaoping Wu[1,4] ✉, and Zutao Zhang[1,2] ✉

[1] School of Mechanical Engineering, Southwest Jiaotong University, Chengdu 610031, China
[2] Chengdu Technological University, Chengdu 611730, China
[3] School of Information Science & Technology, Southwest Jiaotong University, Chengdu 611756, China
[4] Yibin Research Institute, Southwest Jiaotong University, Yibin 644000, China
[5] School of Design, Southwest Jiaotong University, Chengdu 611756, China

Cite this article: *Nano Research*, **2025**, *18*, 94907287. https://doi.org/10.26599/NR.2025.94907287

ABSTRACT: Effective monitoring of mining machinery is of great significance. Sensor nodes, which form the basis of the mine's digital twin system, often face issues of poor sustainability. Therefore, this study introduces a self-powered triboelectric nano-sensor (STNS) enabled digital twin for self-sustained machine monitoring in smart mine. The STNS is designed with three mutually perpendicular sensor units to ensure responsiveness to vibrational energy sources from different directions. Compared to conventional spring-assisted triboelectric nanogenerator (TENG) structures, it exhibits higher frequency adaptability and bandwidth. For a 2 mm amplitude, the STNS responds to frequencies above 10 Hz, with a frequency linearity error rate of less than 0.05%. Utilizing deep learning, the STNS detects various vibrational parameters with an accuracy of ±1 Hz for frequency and ±1 mm for amplitude. A real-time monitoring system based on a deep learning model was constructed and successfully demonstrated for real-time monitoring of amplitude, frequency, and tilt angle. With STNS installed on vibration motor, real-time recognition of the five operating states of the vibration motor and real-time digital twin monitoring were realized. By large-scale distributed deployment of STNS devices, a self-sustained smart mine digital twin ecosystem can be constructed at a lower cost.

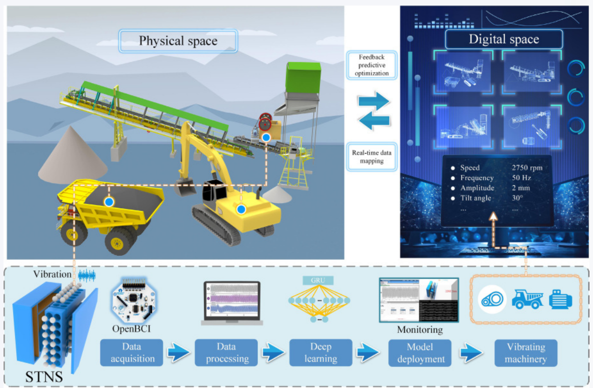

KEYWORDS: digital twin, smart mine, triboelectric nanosensor, deep learning, vibration monitoring

1 Introduction

With the development of information technology, the traditional mining industry is gradually entering the era of artificial intelligence [1]. Mining machinery as an indispensable tool in the mining process, the stability of its performance and operational efficiency is directly related to the safety and productivity of mining operations. However, due to the harsh mining environment and the complexity of operating conditions, machinery frequently faces various faults and wear issues. These not only increase maintenance costs but can also lead to serious safety accidents. Therefore, effective monitoring and management of the operational state of mining machinery, ensuring its operation in an optimal state, are of great importance. Aiming to intelligently maintain mine machinery, digital twin technology offers an effective strategy. Digital twins enable seamless integration of data between physical systems and virtual systems, considered the optimal technology for merging the physical world with digital space [2], featuring virtual-real mapping and data-driven characteristics. With digital twins, maintenance personnel can quickly pinpoint machinery faults without the need for onsite physical operations [3, 4]. To establish a highly interconnected intelligent mining digital twin ecosystem, the widespread distribution of sensor nodes has become fundamental to ensuring seamless integration of information flow and data interchange. With breakthroughs in advanced sensing technologies [5], highly

Received: November 15, 2024; **Revised:** January 4, 2025
Accepted: February 6, 2025

✉Address correspondence to Zutao Zhang, zzt@swjtu.edu.cn; Xiaoping Wu, wuxiaoping@swjtu.edu.cn

integrated monitoring systems are capable not only of capturing detailed data from complex environments but also of implementing these data in digital twin models, providing real-time monitoring and operational functionalities for sectors such as manufacturing [6], logistics [7], and smart cities [8]. These sensor nodes, characterized by distributed dispersion and low power consumption, pose a challenge for existing battery-dependent mine sensor systems in supporting sensor network operations and achieving long-term sustainability. Therefore, developing artificial intelligence-enabled sensors with prolonged endurance capabilities is crucial for building an effective mine digital twin infrastructure. They ensure the continuity and long-term stability of the mine machinery monitoring systems, thereby ensuring seamless interfacing and efficient operations between the digital and physical world.

Mining machinery generally produces vibrations during operation, which, on the one hand, typically accompany energy release that can be captured and utilized to directly power sensor nodes. On the other hand, vibrations also serve as carriers of information, reflecting many details from the vibration source. By extracting this information, it is possible to monitor, diagnose, and control mining machinery. Thus, we can collect vibrational energy and signals from mining machinery to develop AI-enabled sensing nodes with self-sustaining capabilities. To endow the developed artificial intelligence sensing nodes with self-powering and self-sustaining capabilities, researchers have explored various energy harvesting and sensing mechanisms, such as electromagnetic [9–11], piezoelectric [12, 13], and triboelectric effects [14–17]. The electromagnetic energy harvesting mechanism generates energy and electrical signals through electromagnetic induction caused by the relative motion between a permanent magnet and a coil [18]. However, this collection mechanism often has a bulky structure and is susceptible to external disturbances [19]. Piezoelectric energy mechanisms are typically effective in applications involving high-frequency vibrations. However, their output voltage is usually very low, requiring an externally powered amplifier to reach the voltage level necessary for precise measurements [20, 21].

Triboelectric nanogenerators (TENGs) operate through contact electrification and electrostatic induction. Sensors based on TENG technology have received widespread attention due to their high sensitivity and excellent output performance [22]. Recent advancements in TENG have demonstrated its applications in monitoring vibrations in railways [23–25], robotic interactions [26], mining machinery [27], bridges [28], and automobile engines [29]. Numerous studies focus on creating different TENG structures to optimize the harvesting of vibration energy and facilitate self-powered sensing. Typically, these TENGs are constructed using spring-assisted mechanisms or cantilever beam designs, which help to increase motion amplitude and boost power output [30]. For instance, Wang et al. [31] designed a dual-spring structure triboelectric sensor capable of measuring high linearity vibration frequencies within the 0–200 Hz range. Tang et al. [32] designed a two-degree-of-freedom vibration triboelectric nanogenerator based on a cantilever beam, where different stiffness designs of the cantilever beams can increase the system's resonance frequency. To further enhance output power and capture vibrational energy and information from multiple directions, researchers have also attempted to design harvesters that can harvest multidirectional vibrational energy. Chen et al. [19] introduced a generator designed to capture low-frequency vibrational energy from horizontal movements in all directions. Pang et al. [33] arranged three TENG units with identical structures in three mutually perpendicular directions to respond to multidirectional vibrations. However, these structures often have a narrow working frequency band and poor sensitivity to external excitation, making them prone to fatigue damage over long periods. Therefore, many studies have introduced non-contact, non-linear magnetic forces to construct magnetic levitation systems that can mitigate these drawbacks to some extent. For example, Jin et al. [34] proposed a porous triboelectric nanogenerator based on magnetic levitation, but such TENGs require precise control of magnetic field strength and positioning, and their design and manufacturing are challenging; magnetic field strengths are easily influenced by external factors and are also non-linear. In recent years, researchers have proposed springless structures, such as the bouncing ball TENG by Du et al. [35] and the honeycomb structure-inspired TENG by Xiao et al. [36], where the ball, once they accumulate enough kinetic energy, are able to detach from the bottom electrode layer. Compared to traditional spring structures, these are more sensitive to vibration, and their operational frequency bands are significantly increased. In recent years, technologies, including deep learning, have been widely applied in vibration condition monitoring. Combining TENG with deep learning and the Internet of Things (IoT) can achieve intelligent vibration monitoring, avoiding the high costs and inaccuracies of manual tracking and significantly enhancing monitoring efficiency. Zhao et al. [37] proposed a self-powered vibration sensor, utilizing TENG and employing neural network algorithms to identify gearbox voltage signals across varying vibration states. Bhatta et al. [38] proposed a self-powered triboelectric vibration sensor made from Siloxene-Ecoflex elastic pillars, which, combined with deep learning methods (LSTM), can accurately identify different mechanical vibration bodies.

In light of the harsh environments at mining sites, digital twin technology enables maintenance personnel to monitor the status of machinery remotely and in real time. Xin et al. [39] proposed a cantilever-structure freestanding triboelectric nanogenerator that can be utilized to construct a digital twin system for structural crack and defect identification. Jin et al. [26] applied TENG sensors to the flexible grippers of robotic arms, enabling the operations of the virtual robotic arms to be displayed through a constructed digital twin system. Yang et al. [40] utilized TENG in smart home applications, where digital twins replicate walking trajectories and dynamic activity states into digital spaces. Figure 1 showcases the key developments and milestones in AI-enabled self-powered sensing vibration monitoring. Zhao et al. [37] developed a self-powered vibration sensor with high sensitivity to monitoring, illustrating a trend from unilateral development to integration of AI and TENG vibration sensors. Since the introduction of TENG by Wang Zhonglin in 2012, AI-enabled TENG has garnered increasing attention. Although little research has been done on the application of TENG to the monitoring of vibration in mining machinery, future TENG sensors are gradually moving towards integration with artificial intelligence, virtual reality, and digital twin technologies.

Despite the widespread applications of TENG in monitoring vibration machines, these related applications still face several challenges: (i) The design of TENG uses mainly spring-assisted structures or magnetic levitation structures, resulting in low-frequency adaptability and narrow bandwidth. (ii) Monitoring direction is singular, and robustness is poor, making multidirectional monitoring unachievable. (iii) After integrating

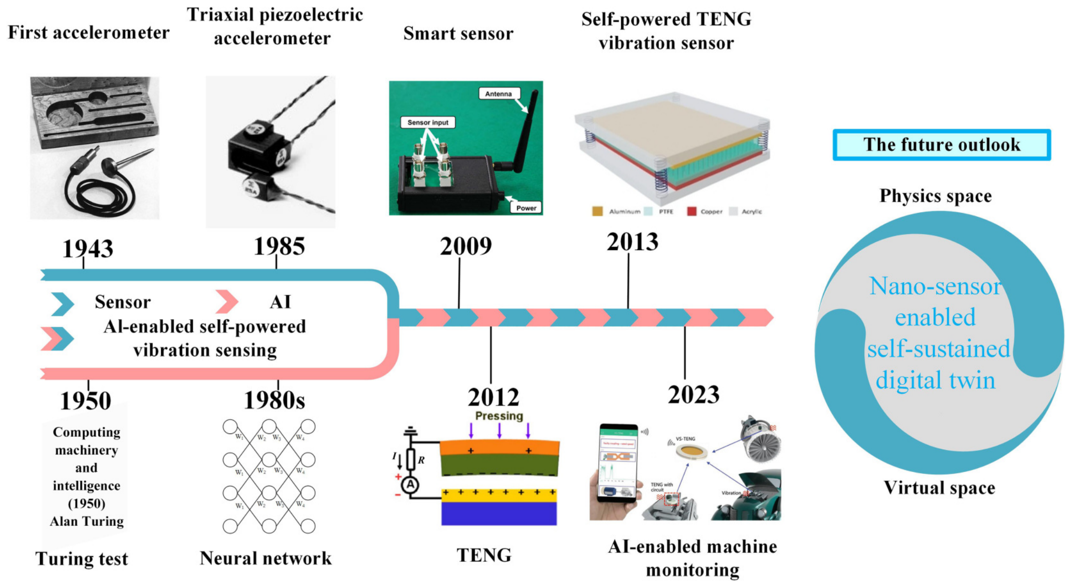

Figure 1 The key developments and milestones in AI-enabled self-powered sensing vibration monitoring. 1943: Reproduced with permission from Ref. [41], © IOS Press 1999. 1985: Reproduced with permission Ref. [41], © IOS Press 1999. 2009: Reproduced with permission from Ref. [42], © Elsevier Ltd. 2009. 2012: Reproduced with permission from Ref. [43], © American Chemical Society 2013. 2013: Reproduced with permission from Ref. [44], © WILEY-VCH Verlag GmbH & Co. KGaA, Weinheim 2013. 2023: Reproduced with permission from Ref. [37], © Wiley-VCH GmbH 2022.

with deep learning, it can only recognize conditions with significant signal differentiation, with few real-time monitoring or diagnostic applications. (iv) Utilizing TENG electrical signals to directly drive virtual space mining machinery and achieve real-virtual mapping remains a challenge. Therefore, this work proposes a self-powered triboelectric nano-sensor (STNS) that enabled digital twin for self-sustained machine monitoring in smart mine. The STNS is based on the principle of a freestanding triboelectric-layer-based nanogenerator, and it is designed with three mutually perpendicular triboelectric sensor units to ensure responsiveness to different directional vibration energy sources. STNS relies on a vibrating ball mechanism, as long as the polytetrafluoroethylene (PTFE) ball overcomes friction or gravity to leave the bottom electrode layer, it can generate an electrical signal. Compared to general spring-assisted TENG structures, it has higher frequency adaptability and bandwidth. Unlike traditional sensors that utilize complex and refined structural designs for direct physical quantity measurement, the STNS employs deep learning technology to detect various parameters, constructing a real-time monitoring system based on the gated recurrent unit (GRU) deep learning model. A graphical user interface can display real-time signals and recognition status. Using this system, real-time monitoring of shaker amplitude, frequency, and tilt angle can be achieved. By installing the STNS on a vibration motor, real-time identification of five different speed states of the vibration motor and digital twin real-time monitoring were realized. Results show that the STNS can realize real-time sensing and detection of vibration parameters and operational states of mining machinery through the integration of deep learning and digital twin technologies, demonstrating potential as a digital twin infrastructure.

2 Results and discussion

2.1 Structure and working principle of STNS

As shown in Fig. 2(a), the diagram of the intelligent mining digital twin system is illustrated. In the physical space, STNS is deployed on various machines within the mine, such as vibrating screens, conveyors, crushers, and mining vehicles, to collect vibrational energy and signal data. Utilizing these data, a self-sustaining mining digital twin system is established that maps the operational status of the mine in virtual space. Concurrently, the operational conditions of machines in virtual space provide feedback predictions and optimizations to the physical space, ultimately achieving intelligent real-time monitoring of these machine statuses. The operational framework of the STNS-based intelligent mining machinery condition monitoring digital twin system is shown in Fig. 2(b). Vibrational machinery, such as vibrating screens, conveyors, crushers, and mining vehicles, serve as the energy sources for STNS, driving the generation of voltage signals that reflect the state of the vibrating body. The STNS features three perpendicular channels, allowing signals to be simultaneously transmitted to the corresponding channels of the OpenBCI. Signals collected by OpenBCI are transmitted to a computer via WIFI, where they undergo processes such as slicing and labelling to form datasets representing different vibrational states. These datasets are then used to train deep learning models, which, once deployed on computers, facilitate convenient real-time monitoring of the vibrating body, including frequency, amplitude, angle, and speed.

The structure and size of STNS are shown in Fig. 3(a), and its compact design allows it to adapt to a wider range of usage environments. It incorporates three structurally identical TENG units arranged in three directions. Each unit is composed of honeycomb frames, PTFE balls, and copper foil. Copper foil is both a conductive layer and a positive friction material. The copper foils in the horizontal units are adhered within their respective frame elements, while in the vertical units, one end of the copper foil is affixed to the shell, and the other end is attached to the cover plate. The PTFE balls, with a diameter measuring 4 mm, function both as oscillators and negative triboelectric layers. Structures other than PTFE balls are fabricated from resin material using three-dimensional (3D) printing. The channels of the honeycomb frame

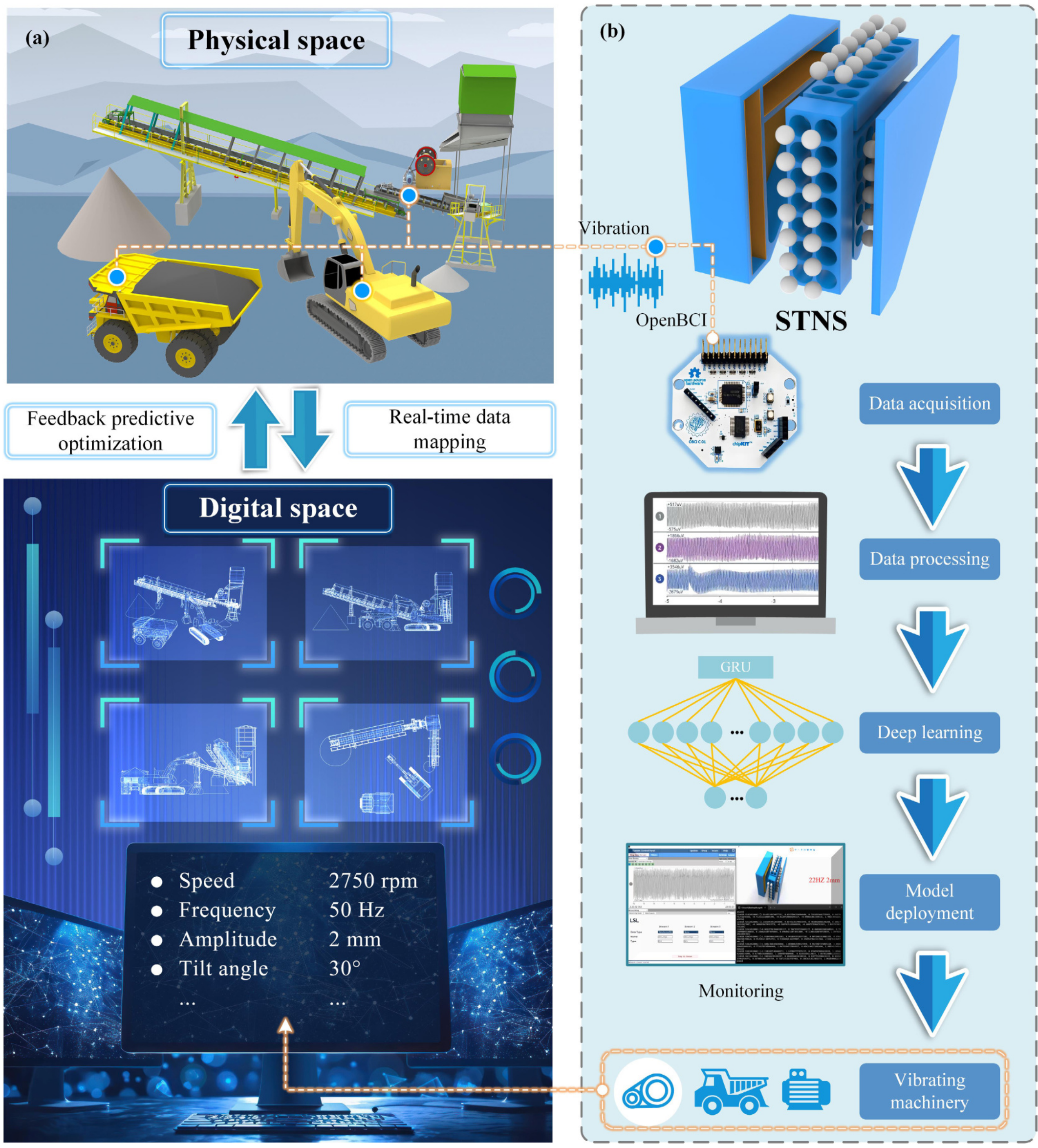

Figure 2 Schematic diagrams of STNS-enabled self-sustained digital twins for machine monitoring in smart mine. (a) Schematic diagram of intelligent mining digital twin system. (b) Flow chart for state monitoring of smart mining machinery based on STNS.

are each 5 mm in diameter and 7.5 mm in depth. Figure 3(b) illustrates both the disassembled and assembled views of the prototype.

The working principle of one channel of STNS is shown in Fig. 3(c). As illustrated in Fig. 3(c)(i), in the initial stage, when the PTFE ball comes into contact with the copper electrode, the copper electrode carries a positive charge, and the surface of the PTFE ball carries a negative charge. Electrons are transferred from the bottom copper electrode layer to the PTFE ball, resulting in the copper electrode being positively charged and the PTFE ball negatively charged. As illustrated in Fig. 3(c)(ii), when the STNS is subjected to external vibrational excitation, the PTFE ball begins to move upwards, separating from the bottom copper electrode layer. During this process, the potential of the top copper electrode is higher than that of the bottom electrode, prompting electrons to start moving from the top to the bottom electrode through the external circuit. In Fig. 3(c)(iii), as the PTFE ball reaches the top copper electrode layer, electrons are transferred to the top copper electrode layer. In Fig. 3(c)(vi), as the PTFE ball moves downward, electrons in the external circuit reverse their direction of transfer. Due to the flow of electrons between the top and bottom copper electrode layers, a stable periodic voltage signal can be generated.

Considering the identical motion of the PTFE balls in each cell of the STNS, as illustrated in Fig. 3(d), the mathematical model of the motion of a PTFE ball in the horizontal direction has been established [45, 46]. The excitation applied to the shell by the shaker is given by Eq. (1)

$$S(t) = A \sin(2\pi f t) \tag{1}$$

where $S(t)$ is the displacement of the PTFE ball's shell, A is the amplitude of forced motion, and f is the frequency of forced motion.

The absolute and relative displacements of the PTFE ball are denoted by $x(t)$ and $y(t)$, respectively, with the relationship (Eq. (2))

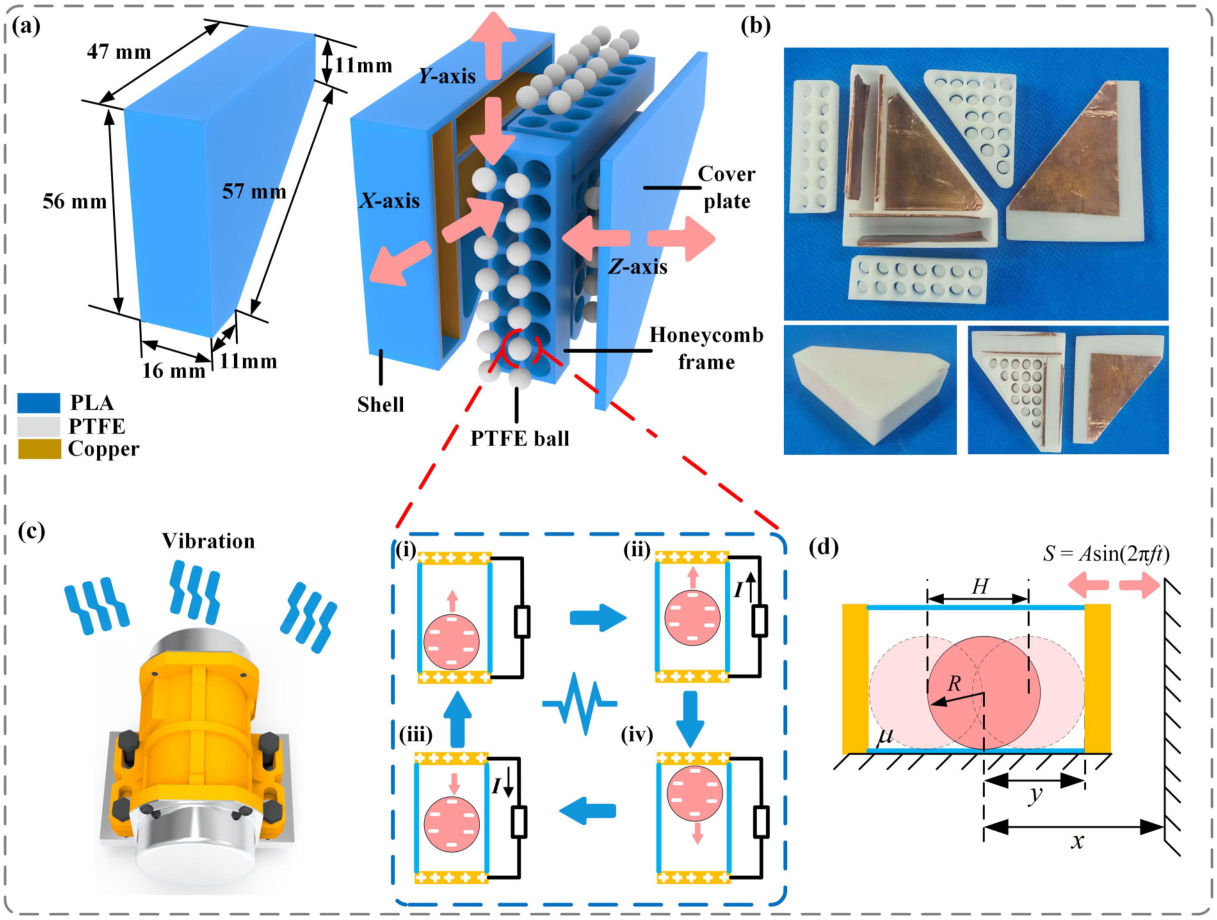

Figure 3 STNS structural design and operating principle. (a) Diagrammatic representation of the STNS structure. (b) Prototype photograph of the STNS. (c) Operating principle of the STNS. (d) Mathematical model of the STNS.

$$x(t) = y(t) + S(t) \tag{2}$$

Considering gravity and assuming a friction coefficient between the PTFE ball and the channel surface, the motion equation for the PTFE ball within the relative coordinate system can be expressed as follows (Eq. (3))

$$\mathrm{sign}(y'(t)) = \begin{cases} 1 & \text{if} \quad y'(t) > 0 \\ 0 & \text{if} \quad y'(t) = 0 \\ -1 & \text{if} \quad y'(t) < 0 \end{cases} \tag{3}$$

$$y''(t) = A(2\pi f)^2 \sin(2\pi f t) + \mu \cdot \mathrm{sign}(y'(t)) \cdot g \tag{4}$$

where sign() is a symbolic function, $y'(t)$ is the relative velocity of the PTFE ball, $y''(t)$ is the relative acceleration of the PTFE ball, μ is the friction coefficient of the channel surface, g is gravitational acceleration.

Use numerical methods for iterative solving, where the time step for each iteration is Δt. t_i is the corresponding time after i time steps. That is: $t_i = i \cdot \Delta t\ (i > 0)$. The initial relative position $y(0)$, initial relative velocity $y'(0)$, and initial relative acceleration $y''(0)$ of the PTFE ball are known. Solve according to the following steps

$$\begin{aligned} y''(t_1) &= A(2\pi f)^2 \sin(2\pi f(t_1)) - \mu \cdot g \\ y'(t_1) &= y'(t_1) + y''(t_1)(t_1 - t_0) \\ y(t_1) &= y(t_0) + y'(t_1)(t_1 - t_0) \end{aligned} \tag{5}$$

$$\begin{aligned} y''(t_i) &= A(2\pi f)^2 \sin(2\pi f(t_i)) - \mu \cdot \mathrm{sign}(y'(t_{i-1}))g \\ y'(t_i) &= y'(t_{i-1}) + y''(t_i)(t_i - t_{i-1}) \\ y(t_i) &= y(t_{i-1}) + y'(t_i)(t_i - t_{i-1}) \end{aligned} \tag{6}$$

H is the stroke of PTFE ball. The conditions for collisions with the plates are

$$y(t_i) = 0 \text{ or } y(t_i) = H \tag{7}$$

Ignoring the duration of impact and considering the simplest impact law using a constant restitution coefficie $\alpha < 1$: When a collision occurs

$$y(t_i) = -\alpha y(t_{i-1}) \tag{8}$$

By iterating the above process, the position of the PTFE ball relative to the shell at any given moment can be obtained. We developed a mathematical motion model of the PTFE ball using MATLAB, with the parameter values used in the calculations listed in Table S1 in the Electronic Supplementary Material (ESM). The relative displacement curves and frequency spectra of the ball under different excitation conditions were obtained (Fig. S1 in the ESM). As shown, the output frequency of the ball is largely consistent with the input excitation frequency. As the vibration frequency increases, the motion curve of the ball becomes more similar to the input sinusoidal excitation function. This demonstrates a good frequency linearity and theoretically proves that the STNS has potential as a vibration sensor.

Based on the principles of contact-separation mode TENGs, the open circuit voltage of the STNS can be written as [47, 48]

$$C = \frac{\varepsilon_0 S}{d_0 + d} \tag{9}$$

$$V = \frac{1}{C}Q + V_{\mathrm{OC}} = -\frac{d_0 + d}{\varepsilon_0 S}Q + \frac{2\sigma x}{\varepsilon_0} \tag{10}$$

where C is the capacitance of the STNS, V is the relative voltage difference between electrodes, R represents the capacitance, Q is the transferred charge, V_{OC} is the open circuit voltage, d_0 is the effective dielectric thickness, d stands for the gap thickness between the two copper electrode layers (the length of the PTFE ball channel), ε_0 is the permittivity in vacuum, S is the surface area of the copper electrode layer, x is the distance separating the copper electrode layer from the surface of the PTFE ball, and σ is the charge density.

The motion simulation of the PTFE ball indicates that, after the STNS reaches stable operation, the motion curve of the ball aligns with the input excitation. Therefore, the motion can be directly regarded as sinusoidal, consistent with the input excitation. The steady-state voltage output $V(t)$ across the resistive load can be expressed as

$$V(t) = \frac{4\sigma A\pi fRC}{\varepsilon_0\sqrt{1+(2\pi f)^2R^2C^2}}\sin(2\pi ft+\varphi) \tag{11}$$

$$\varphi = \arctan\left(\frac{1}{2\pi fRC}\right) \tag{12}$$

In the Eq. (12), φ represents the phase angle.

To validate the above theoretical predictions, the input frequencies during the stable operation of the STNS were selected, and mathematical calculations were performed using MATLAB. The parameter values used in the calculations are listed in Table S2 in the ESM, with the corresponding results shown in Fig. S2 in the ESM. The calculated theoretical STNS voltages were 8.6 V at 2 mm/30 Hz and 11.0 V at 2 mm/40 Hz.

2.2 Experiment and performance of the STNS

As shown in Fig. 4, to evaluate the performance of the STNS and verify its feasibility for application in a self-sustaining digital twin system, a series of experiments were conducted using both a shaker and a vibration motor as the vibration sources. The shaker experiment aimed to test the electrical output characteristics of the STNS and demonstrate real-time monitoring of amplitude, frequency, and angle. The vibration motor experiment

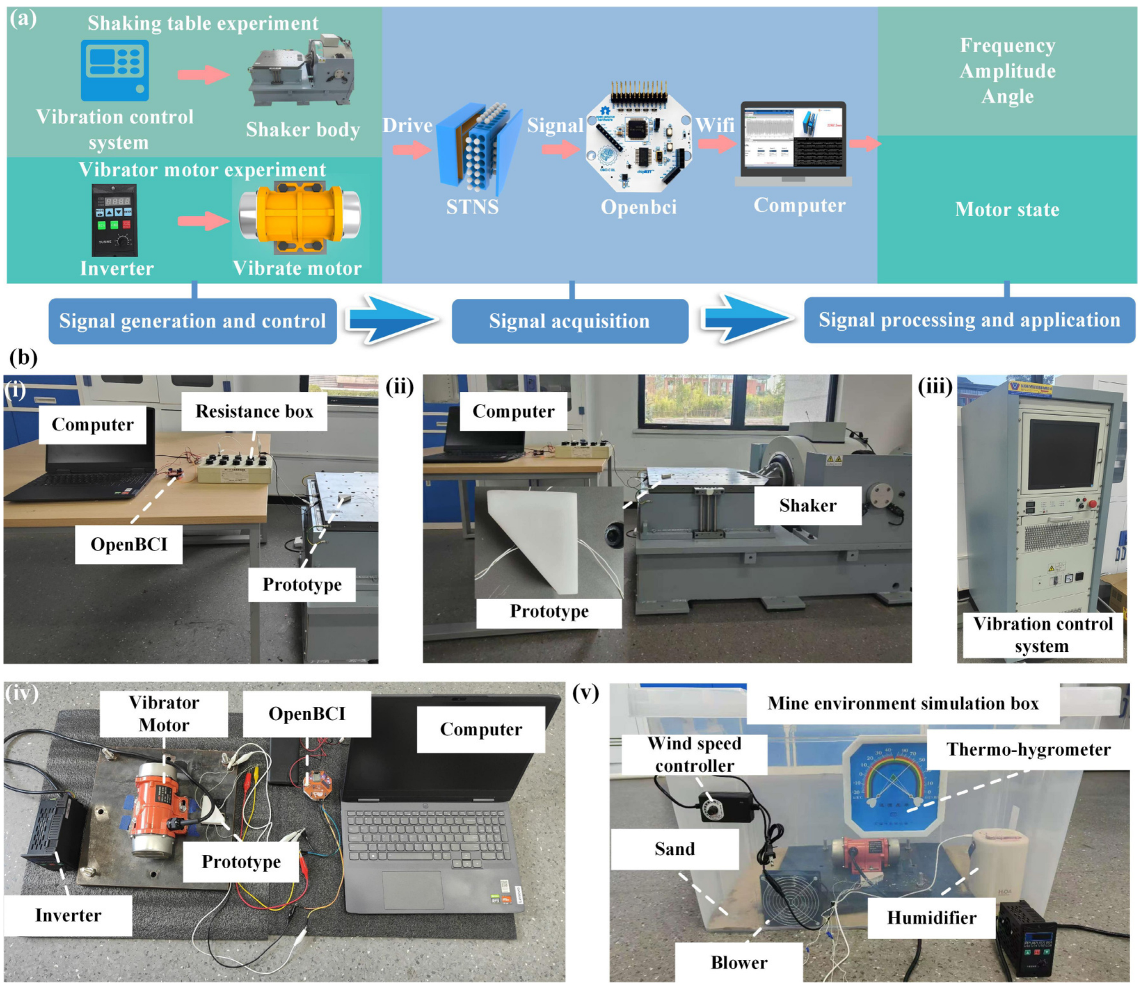

Figure 4 Experimental procedure and details display. (a) Experimental procedure. (b) Details of the shaker experiment and vibration motor experiment: (i) detailed diagram of the shaker experiment; (ii) panoramic view of the shaker experiment; (iii) shaker vibration control system; (iv) details of vibration motor experiment; (v) state monitoring of vibrating motor in a simulated real mine.

demonstrates the practical applicability of STNS by monitoring the vibration characteristics of the motor and thus determining its operating status. The experimental procedure, as shown in Fig. 4(a), can be divided into three stages: signal generation and control, signal acquisition, and signal processing and application. For signal generation, vibrations were produced by the shaker and vibration motor. The vibration of the shaker was controlled by its own vibration control system, while the vibration of the vibration motor was controlled via an inverter. The STNS was fixed to the vibration sources using 3M's VHB 4910 double-sided nano adhesive (performance parameters in Table S3 in the ESM). In consideration of the harsh mining environment, we also designed an STNS with mounting bolt holes, as shown in Fig. S3 in the ESM. However, in this experiment, the VHB 4910 double-sided nano-adhesive was sufficient for fixing, and the mounting bolt holes required additional drilling, so only the version of STNS without bolt holes was used for the experiment. The STNS and OpenBCI were connected by wires, allowing the vibration signals generated by the STNS to be transmitted via the WIFI module in OpenBCI to the computer for visualization and signal acquisition. In the signal processing and application stage, to truly reflect the sensing performance of STNS, we did not perform noise reduction, filtering and other processing on the collected signals, and directly used the raw STNS signals collected by OpenBCI for electrical analysis and deep learning model training.

In the shaker experiment (Figs. 4(b)(i)–4(b)(iii)), the vibration control system generates a sine wave signal, which is then amplified to drive the shaker for single-degree-of-freedom motion with adjustable frequency and amplitude. Using the shaker, we tested the electrical characteristics of a single channel of the STNS under varying frequencies, amplitudes, angles (controlled using an angle controller, as shown in Fig. S4(a) in the ESM), and resistances. To investigate the impact of wind, sand, and temperature-humidity conditions typical of a real mining environment on the performance of the STNS, we developed a simplified mining environment simulation test box (Fig. S4(b) in the ESM). This setup allowed us to test the effects of temperature and humidity in a wind-sand environment on the electrical performance of the STNS. Finally, durability tests of the STNS were also conducted.

In the vibration motor experiment (Figs. 4(b)(iv) and 4(b)(v)), we demonstrated real-time condition assessment and digital twin-based monitoring of the vibration motor using the STNS. The vibration motor was mounted with four bolts on a steel plate with dimensions of 300 mm × 300 mm × 25 mm (length × width × thickness) and a weight of 25.5 kg. To minimize vibrations and their impact on the ground, the motor and its base were placed on a foam board. The vibration state of the motor was adjusted using an inverter and the STNS was fixed to the base plate. The electrical signals from the three channels of the STNS were acquired simultaneously using OpenBCI and then transmitted to a computer via WIFI for subsequent deep learning processing and digital twin applications. Table S4 in the ESM provides the detailed specifications of the main device used in the experiment.

Since the voltage range of OpenBCI is 0–5 V, the voltage dividing is achieved by connecting a 3 MΩ resistance in series during the electrical characteristic test, as shown in the wiring diagram in Fig. S5 in the ESM. Therefore, in the shaker experiment, all the measured voltage values are the voltage values corresponding to the 3 MΩ resistance after voltage division. Figure 5(a) illustrates the voltage measurements of the STNS's X-axis channel under 3 MΩ and open circuit conditions at a 15 Hz frequency. It is evident that under open circuit conditions, the voltage and RMS values are approximately 3 times those measured at 3 MΩ. As shown in Fig. 5(b), a Fourier transform of the STNS signal under a 3 MΩ load at 30 Hz reveals a main frequency of 30.0543 Hz, closely matching the excitation frequency, with 50 Hz representing external power interference. In addition, Fig. S6 in the ESM shows the spectrograms of the STNS system at 15, 20, and 25 Hz. It can be observed from the plots that the dominant frequency is essentially the same as the excitation frequency, which indicates that the STNS is able to respond accurately to the applied vibration frequency.

Since the primary target applications of the STNS are machinery with high overall vibration amplitudes in intelligent mining environments, such as vibrating screens and crushers, a higher vibration amplitude of 2 mm was selected for testing in this experiment. For the frequency range of 10 to 50 Hz, the output voltage of the three channels of the STNS was measured, and the results are shown in Fig. 5(c). At frequencies below 25 Hz, all three channels exhibit low signal amplitudes due to the device operating in an independent contact separation mode, where the movement distance for the PTFE ball measures 3.5 mm. At these lower frequencies, most of the PTFE balls do not contact the copper foils on either end, resulting in minimal electron transfer. As the frequency increases above 25 Hz, the signal amplitude significantly grows. Between 25 and 40 Hz, the PTFE balls make full contact and collide with the copper foils, resulting in a gradual increase in the voltage amplitude. Above 40 Hz, the effective contact area between the PTFE balls and the copper foil is maximised and the voltage amplitude saturates. Voltage amplitude exceeding 3 V after STNS is fully stabilised, which translates to an open circuit voltage of approximately 9 V, which is similar to the previous voltage simulation (Fig. S2 in the ESM). These results indicate that under low-amplitude vibration conditions, the device can stably harvest vibrational energy and extract signals once the vibration frequency exceeds a certain threshold. Figure 5(d) show that when the vibration frequency is maintained at 20 Hz, the voltage amplitude exhibits similar trends to changes in vibration amplitude as observed with changes in frequency. At vibration amplitudes below 2.5 mm, the PTFE balls in the channels remain stationary or in a slight trembling state due to friction, resulting in minimal contact with the copper foils and low signal amplitudes in all three channels. Between 2 and 4 mm, the PTFE balls make sufficient contact with the copper foils, and the contact area gradually increases. Under a constant frequency, the vibrational acceleration linearly increases with the vibration amplitude, thereby observing larger voltage changes. At amplitudes greater than 4.5 mm, the effective contact area between the PTFE balls and the copper foils reaches its maximum, and the output voltage amplitude tends toward saturation.

As illustrated in Fig. 5(e), at a steady vibration of 20 Hz/2 mm, the signal amplitude of the three channels decreases as the STNS tilts. Below an angle of 30°, the amplitude gradually diminishes. However, as the angle exceeds 30°, the signal amplitude rapidly decreases. This is mainly because the PTFE balls reach a critical angle where they can no longer make contact with both the upper and lower copper foils, only making contact with the lower foil, resulting in a rapid decrease in signal amplitude, ultimately reaching the lowest point at 90°. Despite this, due to the excitation of the shaker, the PTFE balls can still oscillate within the channel and momentarily detach from the lower copper foil surface, thereby

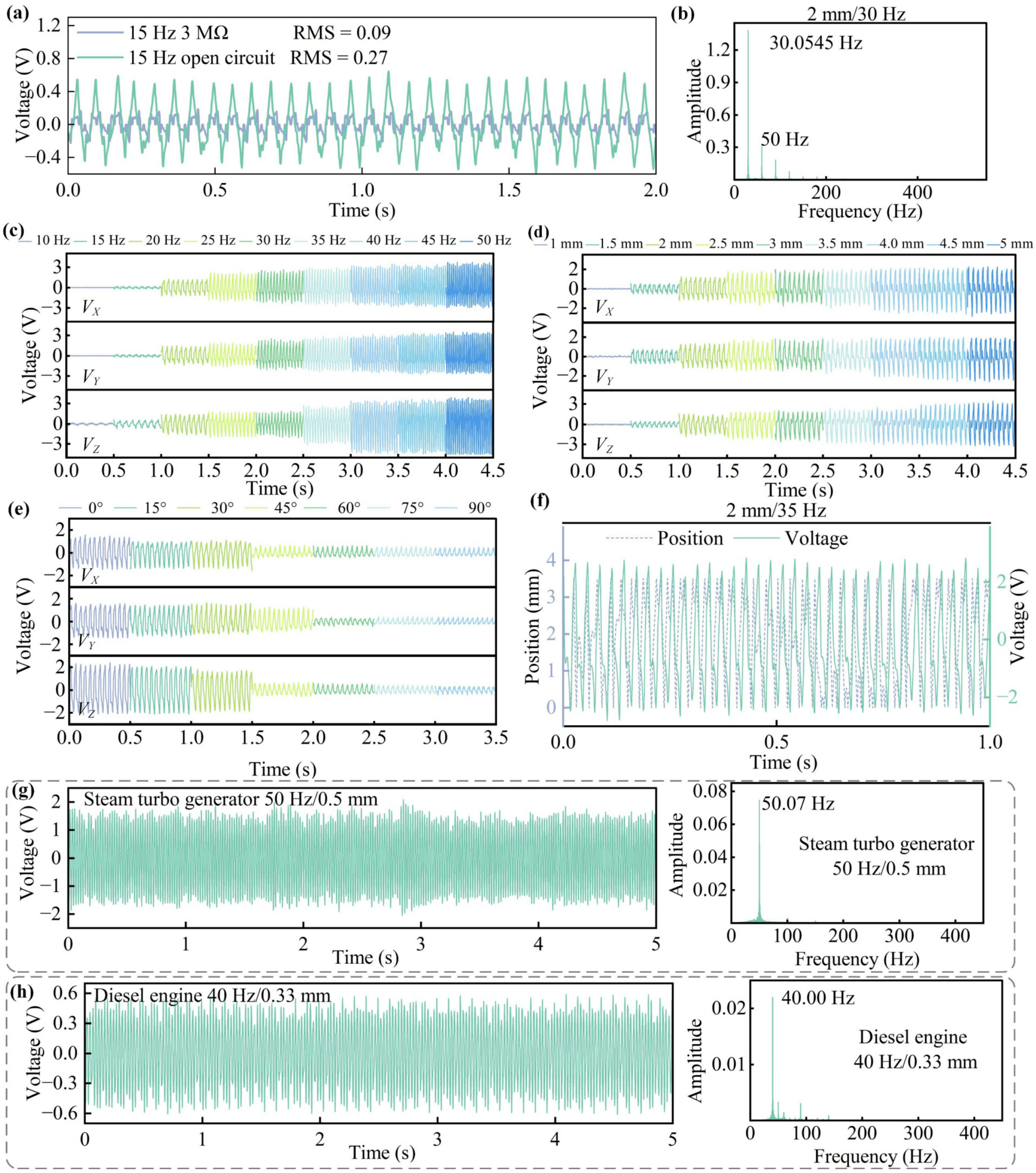

Figure 5 Vibration output performance of STNS. (a) Open-circuit and 3 MΩ load voltages of STNS at 15 Hz. (b) Spectrum of the load voltage under a 3 MΩ load at 30 Hz for STNS. (c) The output voltage under a 3 MΩ load from the STNS across various frequencies, with an amplitude of 2 mm. (d) Voltage output of STNS under a 3 MΩ load at various amplitudes with frequency of 20 Hz. (e) STNS voltage output at 3 MΩ, 2 mm/20 Hz, different angles. (f) Comparison of simulated and actual output voltages for PTFE ball motion at 3 MΩ, 2 mm/35 Hz. (g) The output voltage of STNS's *X*-axis at 0.5 mm/50 Hz. (h) The output voltage of STNS's *X*-axis at 0.33 mm/40 Hz.

still generating a signal that reflects the vibrational state. This is the basis on which angle monitoring experiment can be conducted. Due to structural design considerations, the *Z*-axis has a larger copper foil area and more PTFE balls, resulting in voltage amplitude consistently higher than the other two channels.

To verify the correctness of the theoretical motion model of the PTFE balls, as shown in Fig. 5(f), we plotted the relative position of the PTFE balls versus the voltage curves under the condition of 2 mm/35 Hz. The results show that the motion curves of the ball as a whole show a high degree of consistency with the voltage output waveform of the STNS. This phenomenon indicates that there is an extremely strong frequency correlation between the STNS signal and vibration. For the characteristics of low-amplitude mechanical vibrations, we selected a diesel engine and a steam turbine generator [49]. After simulating their vibrations using a shaker, the output voltage and spectrum of the STNS under these conditions were tested (Figs. 5(g) and 5(h)). The experimental results show that the STNS still has good response capability under low-amplitude mechanical vibration conditions, thus further verifying its applicability to complex vibration environments. In order to verify the feasibility of using the STNS in a real mine environment, the STNS was placed in a mine environment simulation box and the blower was turned on at all time during the test to simulate mine wind and sand. The output voltage of STNS under various temperature and humidity conditions was tested, and the test results (Fig. S7 in the ESM) showed that the output voltage waveform of STNS remained stable between 25%–85% humidity; STNS showed a slight decrease in temperature at 20 °C compared to 10 °C, and was essentially the same at 20 and 35 °C. The overall STNS was basically in the range of temperature 10–35 °C. It is consistent with the results of Yu et al. [50] (friction electricity between FTFE and Cu remains stable between 20%–90% humidity) and Lu et al. [51] (friction electricity between FTFE and Al remains stable between 20–100 °C).

To investigate the self-sensing capability of the STNS, the signal-to-noise ratio (SNR) under various frequencies, amplitudes, and tilt angles was statistically analyzed. At frequencies ranging from 10 to 50 Hz (Fig. 6(a)), the lowest SNR recorded was 2.2 dB, with the SNR progressively increasing to a stable maximum of 296 dB as the vibration frequency increased. At a constant frequency of 20 Hz

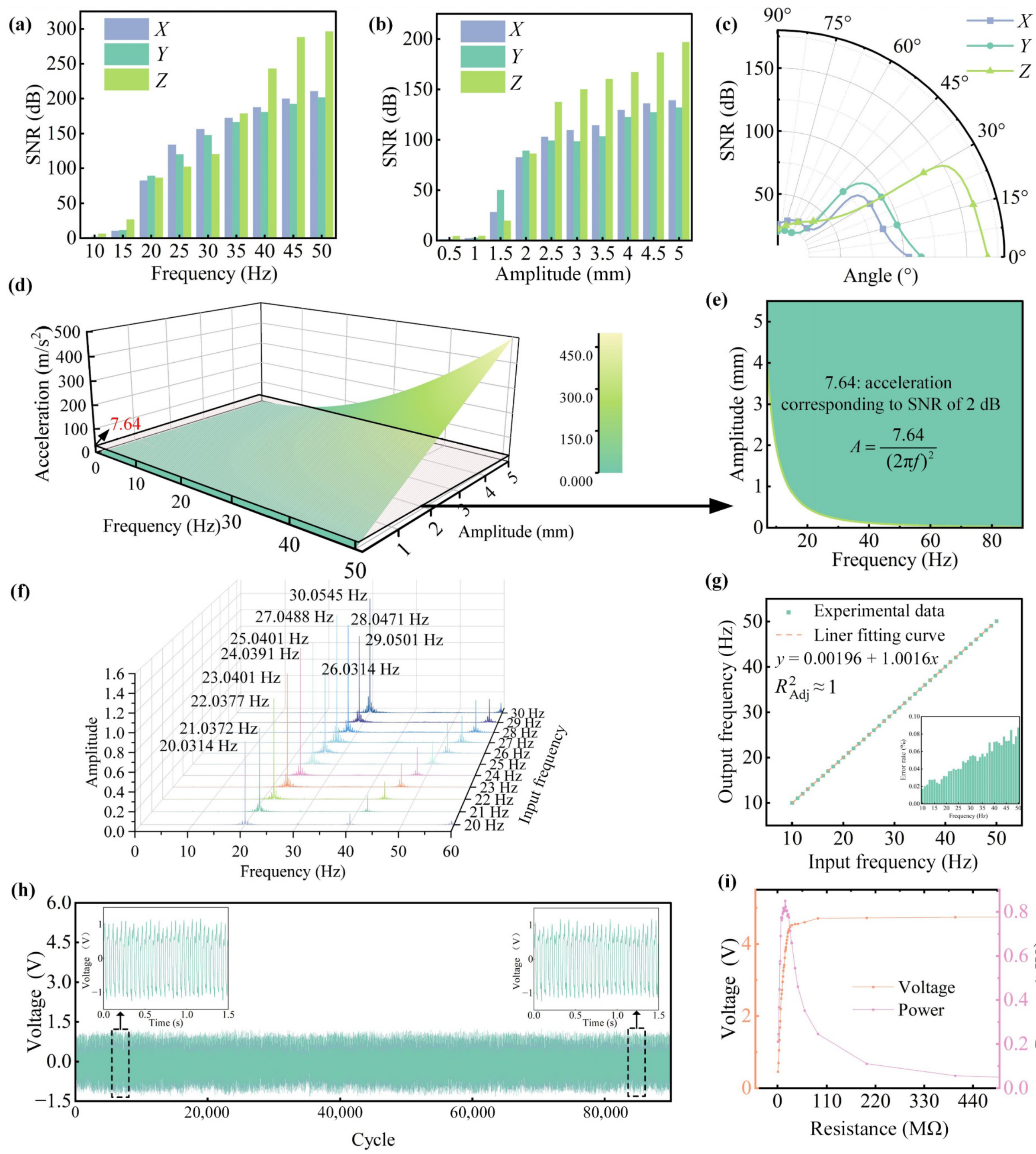

Figure 6 Sensing characteristics of STNS. (a) SNR of STNS at various frequencies with amplitude of 2 mm. (b) SNR of STNS at different amplitudes with frequency of 20 Hz. (c) SNR of STNS at different angles with a fixed vibration frequency of 20 Hz and amplitude of 2 mm. (d) Relationship between maximum vibration acceleration, vibration amplitude, and vibration frequency. (e) Operational response range of STNS. (f) Spectrum corresponding to STNS in the 20–30 Hz frequency range. (g) Frequency linearity of STNS in the 10–50 Hz range. (h) Stability test (90,000 cycles). (i) Output power and values under different loads.

with amplitudes from 0.5 to 5 mm (Fig. 6(b)), the minimum SNR was 2.09 dB, and the maximum SNR reached 296 dB. As the angle incrementally increased from 0° to 90° (Fig. 6(c)), the SNR decreased from 266 to 20 dB, yet maintained normal operation at 90°.

The maximum vibration acceleration of the STNS in the horizontal direction can be expressed as Eq. (13)

$$a = A(2\pi f)^2 - \mu g \tag{13}$$

This relationship between vibration acceleration, amplitude, and frequency is illustrated in Fig. 6(d). Given the fixed travel of the PTFE balls, it is evident that stable signal generation can occur once the vibrational acceleration of the PTFE balls exceeds a certain threshold. If the minimum SNR of a channel exceeds 2 dB, STNS can be defined as being capable of generating a stable signal. Figure 6(b) shows that at a frequency of 20 Hz and an amplitude of 0.5 mm, the Y-axis channel achieved an SNR of 2.09 dB. Theoretically, as long as the acceleration of the given excitation exceeds this value, the STNS can operate stably, as demonstrated by the response curve in Fig. 6(e). The STNS possesses a response bandwidth far exceeding that of other similar types of energy harvesting devices. Unlike typical resonant systems, the STNS responds to vibrational excitation once the vibration acceleration exceeds a certain value. Moreover, by reducing the friction coefficient in the channels, further improvements in response bandwidth are anticipated.

As shown in Fig. 6(f), a frequency domain decomposition of the X-channel signal from 20 to 30 Hz revealed that all output signal working frequencies were close to the excitation frequency. STNS's signal frequency was used as the input frequency for comparison and linear fitting with the shaker's output frequency (Fig. 6(g)). Results indicate a very high linearity within the 10–50 Hz vibration frequency range, with a fitted R-squared value nearly equal to 1. The frequency monitoring error rate of the device is less than 0.2%. As depicted in Fig. 6(h), a stability test was conducted over 90,000 cycles at a frequency of 25 Hz and an amplitude of 2 mm. The outcome revealed that the output voltage waveform of the STNS was consistent throughout extended use, confirming its stability and durability. To determine the optimal load resistance, a resistance box was connected to the circuit, and the output voltage and power across various load resistances were recorded, as shown in Fig. 6(i), with the optimal load resistance being around 17 MΩ.

2.3 Intelligent sensing of the STNS

By integrating time-domain and frequency-domain analyses, we observed that the device's output signals significantly reflected multiple physical characteristics of the test object, including amplitude, frequency, and tilt angle. Based on these findings, we designed a real-time monitoring system using a GRU-based deep learning model aimed at real-time monitoring and analysis of the vibrational states of the test objects. This system can achieve real-time recognition of the amplitude, frequency, and inclination of the monitored vibrational body.

The STNS's three channels can simultaneously acquire vibration signals in three mutually perpendicular directions, ensuring responsiveness to excitation from different directions and thus enhancing reliability in practical applications. To facilitate a real-time graphical display of the monitoring target by the STNS, a graphical user interface was developed, which can display both the raw output signals and the recognized states. The trained GRU model then identifies these signals to assess the operating status of the device and wirelessly transmits this information to the user. During the deep learning model's training phase, we collected 24 sets of signals ranging from 20–25 Hz in frequency and 2–4 mm in amplitude, with intervals of 1 Hz/1 mm. To reduce the overall data volume, data collection was performed at a sampling rate of 250 Hz, with each signal collection lasting 80 s and comprising 20,000 data points. The dataset was divided into three subsets: training, validation, and test, following a distribution ratio of 7:1.5:1.5.

The detailed structure of the GRU model is shown in Fig. 7(a), and the data processing steps are depicted in Fig. 7(b). We used a sliding window technique to segment the data, with each window consisting of 200-time steps and a step size of 2, followed by data shuffling to increase diversity and prevent overfitting due to the high correlation between adjacent data slices. The model architecture includes a GRU layer with 64 hidden units and implements a 0.2 dropout rate on both input and recurrent layers to reduce overfitting. The output layer is a fully connected layer equipped with 24 units and a softmax activation function designed for a 24-class classification problem. Additionally, L2 regularization was introduced in the output layer to prevent overfitting further. The entire training process encompassed 250 epochs, processing 2800 samples per epoch.

The confusion matrix is shown in Fig. 7(c). The network model's accuracy and loss curves during training iterations are displayed in Fig. 7(d). From the 200th iteration onward, the training accuracy and loss approached convergence and declined slowly, achieving a final training accuracy of 98.52% and a test accuracy of 97.42%. Test results demonstrate that the developed deep learning model can accurately recognize vibrational signals with a precision of ±1 mm and ±1 Hz. This represents a significant improvement over previous studies, which were only capable of monitoring a broad range of frequencies or simple on/off states of mechanical devices. To demonstrate the real-time monitoring capabilities of the constructed system, as shown in Video S1 in the ESM, we achieved real-time recognition of five different amplitudes from 2 to 5 mm at a frequency of 25 Hz and five different frequencies from 20 to 24 Hz at an amplitude of 2 mm was performed.

Given its distinctive signal characteristics under different tilt angles, the STNS can also serve as a vibration machine angle monitoring sensor node. Similarly, using the three channels of the STNS, we collected five sets of signals, including noise under conditions from 0° to 90° at 25 Hz, with 30-degree intervals. The trained confusion matrix and accuracy and loss curves are shown in Figs. 7(e) and 7(f), achieving a final training accuracy of 99.87% and a test accuracy of 99.62%. Post-training, real-time deployment demonstrations were conducted, as shown in Video S2 in the ESM.

2.4 State real-time monitoring of the vibration motor based on STNS

In the mining industry, the application of vibration motors is extremely widespread, primarily used for the screening, conveying, and grading of ores at critical stages. To validate the performance and practicality of our designed sensors in actual applications, we selected a vibrating screen from the mining industry as the demonstration machinery. Figure 8(a) illustrates the structure of a common vibrating screen and the installation location of the core component, the vibration motor. We installed the STNS on the vibration motors to identify and monitor different machine states

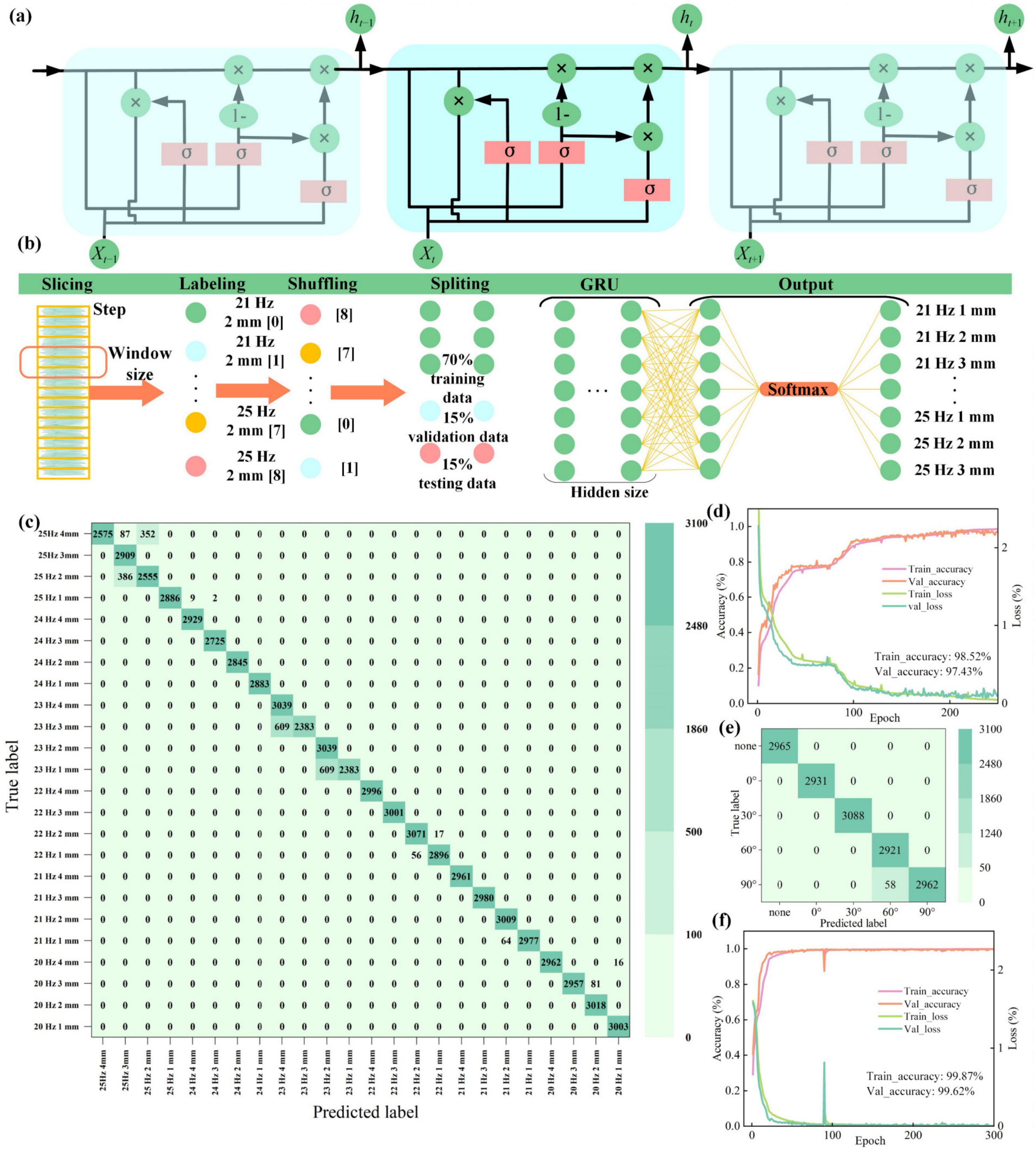

Figure 7 Real-time vibration monitoring based on GRU. (a) Detailed structure of the GRU model. (b) Voltage data processing workflow. (c) Confusion matrix for 24 combinations of frequencies and amplitudes. (d) Training accuracy and loss function for 24 combinations of frequencies and amplitudes. (e) Confusion matrix for angle states. (f) Training accuracy and loss function for angle states.

during operation. A converter is used to regulate the frequency of the vibration motor's operating current, thus achieving speed regulation. The wiring of STNS and OpenBCI is shown in Fig. S8 in the ESM. Three channels were used to train the model for vibration motor state recognition, collecting 20,000 data points over 80 s for each of the five operational states of the motor. The voltage signals of different speeds across the channels, as shown in Figs. 8(b)–8(d), reveal that vibrations of the motor are primarily concentrated in the *Z*-axis and *X*-axis directions, dictated by the structure of the vibration motor. As the speed increases, the amplitude of the channel signals shows a significant variation. However, when the speed exceeds 2353 rpm, although the signals still differ considerably, they become difficult to distinguish through simple observation alone. A GRU model was employed for training, with parameters adjusted based on actual performance. After fine-tuning, each sliding window was set to 200-time steps with a stride of 1, and the model architecture included one GRU layer with 64 hidden units. Following training completion, the confusion matrix, as shown in Fig. 8(e), and the accuracy and loss curves, as depicted in Fig. 8(f), indicated a training accuracy of 100% and a testing accuracy of 100%. The trained model was deployed in the developed real-time monitoring system, with real-time monitoring

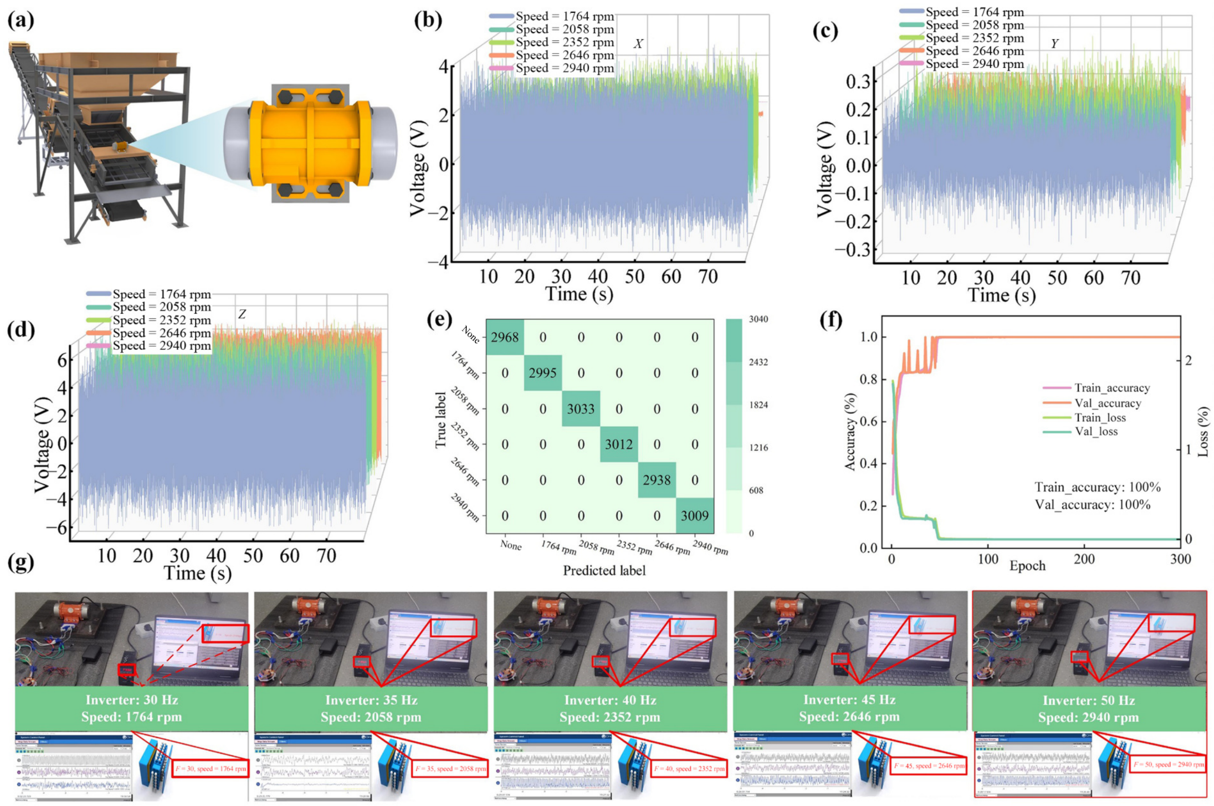

Figure 8 State real-time monitoring of the vibration motor based on STNS. (a) Schematic illustration of the vibrating screen structure and the installation location of the core component, the vibration motor. (b)–(d) Voltage values across three channels at various speeds. (e) Confusion matrix for deep learning-based speed recognition. (f) Training accuracy and loss function for deep learning-based speed recognition. (g) Vibration motor real-time condition monitoring.

results depicted in Fig. 8(g). A live demonstration video is available in Video S3 in the ESM, ultimately achieving precise identification of five speed states of the motor ranging from 1764 to 2940 rpm.

2.5 Demonstration of digital twin system for monitoring mining machinery based on STNS

Mining environments are often considered extreme work conditions with high potential hazards. To achieve remote visual monitoring of mines, there is an urgent need for real-time reconstruction of the mine conditions based on digital twins. Consequently, the proposed STNS can be used as a sensor node, deployed on a large scale in harsh mining conditions, to establish an industrial AIoT for collecting essential multimodal information. As illustrated in Fig. 9(a), multiple STNSs are employed to form a wireless sensor network for mining machinery. These STNSs collectively constitute the infrastructure of a mining digital twin system. The signal data collected by the STNSs can be transmitted to cloud servers at high speed and low latency via emerging 5G technology. Through this data, real-time virtual reconstruction of mining machinery is achieved, thereby enabling the monitoring of mechanical status and the risk assessment of environmental conditions.

Figure 9(b) illustrates the basic working principle of the mining machinery monitoring digital twin system constructed based on STNS. In the physical space, a vibration motor is used to simulate the vibration of a vibrating screen in the virtual space. In the initial phase, the training data is collected by the STNS and processed using deep learning algorithms for model training. After completing the training and deployment of the deep learning model, the system is able to make predictions based on real-time vibration motor signals and visualise the predictions. In the specific implementation process, the trained deep learning model is first loaded into the Unity environment, the real-time data is input into the constructed real 3D model of the mine for inference and analysis, and then the inference results are fed back into the Unity scene to present the mechanical status in real-time, to realise the digital twin visualisation monitoring of the mining machinery.

Figure 9(c) illustrates the practical application of the digital twin-based system for mining monitoring during test. The vibratory motor test bench is placed in a mine environment simulation box to simulate the real mine environment. This demonstration features real-time mirroring of the vibration motor's operational state on a large screen within the monitoring center, enabling immediate observation and analysis of mining operations. The performance of the STNS-based mining machinery monitoring digital twin system under different operational states was tested by controlling the output of the vibration motor through a converter, thus controlling its various operating states. Experimental results, as shown in Fig. 9(d) and demonstrated in Video S4 in the ESM, indicate that the proposed monitoring system for mining machinery with digital twin can accurately identify the five operating states of vibration motors and realise their real-time mapping in the digital twin model. This enables real-time assessment of the operational status of mining machinery and achieves the purpose of remote monitoring and early warning. Additionally, the signals of different fault states of mining machinery are also distinctly identifiable. If STNSs are deployed on a large scale within mining machinery as part of the AIoT infrastructure, real-time monitoring and fault diagnosis of the entire mining machinery can be achieved.

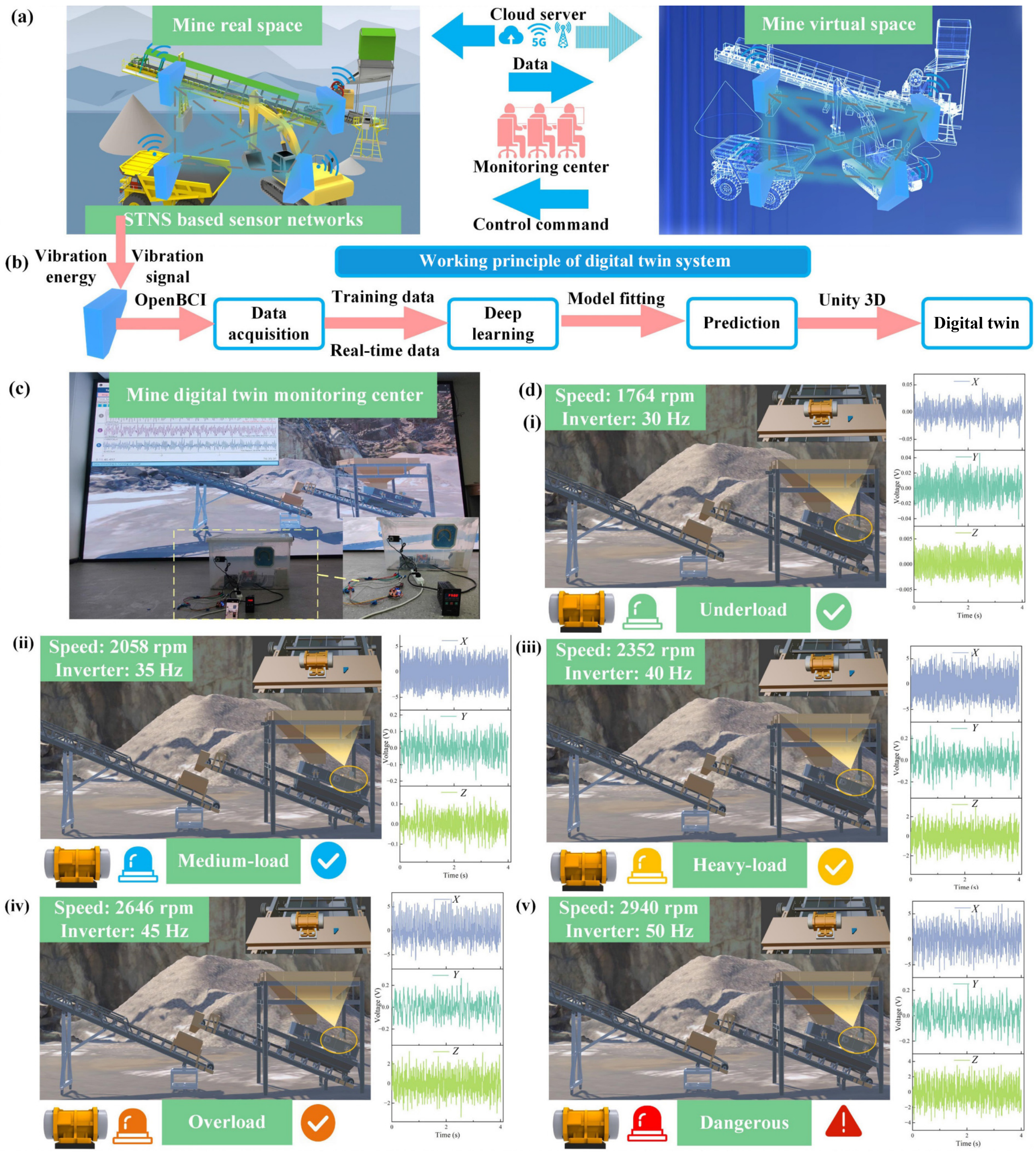

Figure 9 Demonstration of the mining machinery monitoring digital twin system based on STNS. (a) Schematic of the large-scale deployment of STNS forming a smart mining ecosystem. (b) Working principle schematic of the STNS-based mining machinery monitoring digital twin system. (c) Live demonstration of the STNS-based mining machinery monitoring digital twin system. (d) Various operational states of the mining machinery monitoring digital twin system.

Along with other self-powered sensors (such as humidity sensors and pressure sensors), a sustainable, low-cost, smart mining ecosystem can be built. As shown in Fig. 10, in addition to smart mine, STNS can also serve as universal vibration sensors. When integrated with digital twins, 5G transmission, and artificial intelligence technologies, these sensors are applicable in areas such as smart factories, smart power systems, smart transportation, and smart wearables. Furthermore, they facilitate the construction of similar self-sustaining digital twin systems and even metaverse world. The proposed STNS has been compared with the existing TENG for vibration monitoring (Table S5 in the ESM). It shows that the proposed STNS has significant advantages and progress in terms of monitoring content, monitoring accuracy, and real-time recognition.

3 Conclusions

In this work, a self-power triboelectric nano-sensor enabled STNS is proposed for machine monitoring in smart mine. The STNS is based on the principle of a freestanding triboelectric-layer-based nanogenerator, designed with three perpendicular triboelectric sensor units to ensure responsiveness to vibrational energy sources in various directions. STNS relies on a vibrating ball mechanism, as

Figure 10 STNS application prospects in the future.

long as the PTFE ball overcomes frictional force or gravity away from the bottom electrode layer, it generates an electrical signal. Compared to conventional spring-assisted TENG structures, it offers higher frequency adaptability and bandwidth. The performance of STNS was tested on a shaker at different frequencies, amplitudes, and angles, with analyses of the SNR, operational response range, and stability. Results demonstrate that STNS exhibits high sensitivity to various frequencies, amplitudes, and angles. The minimum operational response of STNS, defined by a SNR greater than 2 dB, was determined through experimental and theoretical analysis. For a 2 mm amplitude, STNS responds to frequencies above 10 Hz with a high linearity ($R \approx 1$) and an error rate of less than 0.05%. Unlike traditional sensors that measure physical quantities directly with complex and refined structural designs, STNS employs deep learning techniques to detect various parameters, achieving recognition accuracies of ±1 Hz for frequency and ±1 mm for amplitude. A real-time monitoring system based on a GRU deep learning model was constructed, with a graphical interface that displays original signals and recognition statuses in real-time. This system was successfully demonstrated for real-time monitoring of amplitude, frequency, and tilt angle on a shaker. To demonstrate the feasibility of using STNS for state monitoring of vibrating machinery, STNS was installed on a vibration motor, collecting STNS voltage signals from five different states of the motor. Using the constructed real-time monitoring system, real-time monitoring of the vibration motor's states was achieved, with a validation accuracy of 100% for the five states on the testing set. This established an STNS-based digital twin monitoring system for mining machinery, experimenting with the virtual reproduction of five states of the vibration motor.

The challenges faced by existing TENG applications for vibration monitoring are discussed in the introduction section, and STNS effectively overcomes these challenges in the following ways: (i) STNS relies on a vibrating ball mechanism, compared to spring-assisted TENG structures, has high sensitivity, high SNR, good frequency adaptability and a wide operating response range. (ii) With three mutually perpendicular channels, STNS can respond to vibration signals in multiple directions simultaneously, providing greater robustness and environmental adaptability. (iii) Combined with deep learning, real-time monitoring accuracies of ±1 Hz for frequency and ±1 mm for amplitude were achieved. (iv) Based on deep learning and digital twin technology, real-time judgment and digital twin real-time monitoring of five states of the vibration motor were experimented with, showcasing the potential for low-cost construction of a self-sustained intelligent mining digital twin system. These results indicate that by large-scale distributed deployment of STNS devices, a low-cost, self-sustaining mining digital twin system can be constructed to achieve smart monitoring of the entire mine.

The research in this work has demonstrated the feasibility of constructing a self-sustaining STNS-based digital twin for mines at a low cost, with the potential to be extended to other similar vibration monitoring areas. However, the large-scale deployment of STNS in smart mine still faces the following potential problems that need to be further explored in future research: (i) Under the complex mining environment, how to achieve stable networking of a large number of STNS nodes is a key challenge. At the same time, the topology of STNS network should be optimised according to the characteristics of mining environment. (ii) In the mining environment, how to achieve efficient and stable wireless long-distance transmission of signals from large-scale STNS nodes while ensuring low latency is another challenge that needs to be solved. (iii) The vibration characteristics of different machinery in mines vary significantly, so targeted research and improvement in system structure design and algorithm optimisation are needed for the characteristics of different machinery.

In response to the above potential problems, we offer the following ideas for future work to collectively address these issues that may also exist in other TENG-based monitoring studies: (i) In order to solve the problem of large-scale STNS networking, future research can extend from single STNS experiments to the networking test of multiple STNS nodes, and optimise the topology of the network by combining it with the complex terrain characteristics of the mining environment, to construct a network system with stronger robustness. (ii) For the characteristics of the mining environment, existing wireless communication technologies can be developed or optimised to achieve the requirements of low-power consumption and long-distance wireless communication. For example, the coverage range of long-distance communication signals is enhanced by introducing relay nodes or relay base stations. At the same time, combined with machine learning algorithms to dynamically optimise the communication path, the communication delay is further reduced and the system performance is improved by selecting the optimal path in real-time. (iii) In the face of the significantly different vibration characteristics of different machinery in the mine, the design parameters of the STNS (e.g., channel stroke, number of PTFE balls, electrode material, etc.) can be adjusted to adapt to the characteristics of different machinery. In addition, a large-scale vibration dataset covering diverse mining machinery should be established, and the multi-task learning method in deep learning should be used to train the model simultaneously to identify the vibration signal characteristics of different machinery, to improve the versatility and accuracy of the algorithm.

Electronic Supplementary Material: Supplementary material (additional figures, tables and videos) is available in the online version of this article at https://doi.org/10.26599/NR.2025.94907287.

Data availability

All data needed to support the conclusions in the paper are presented in the manuscript and the Electronic Supplementary Material. Additional data related to this paper may be requested from the corresponding author upon request.

Acknowledgements

This work is granted by the National Natural Foundation of China (No. 51975490), the Science and Technology Projects of Sichuan (Nos. 23QYCX0280 and 2024JDRC0094), the Science and Technology Projects of Yibin (Nos. 2021ZYCG017, 2023SJXQYBKJJH005, SWJTU2021020001, and SWJTU2021020002).

Declaration of competing interest

All the contributing authors report no conflict of interests in this work.

Author contribution statement

J. P. J.: Writing – original draft, conceptualization, investigation methodology, visualization. C. L. F.: Data curation, software, validation. H. Y. C.: Methodology, visualization. F. W.: Conceptualization, formal analysis, investigation, methodology. X. H. F.: Conceptualization, methodology. H. Y. P.: Conceptualization, formal analysis, supervision, validation. C. J. X.: Methodology, resources, software. X. P. W.: Writing – review & editing, methodology, project administration, supervision. Z. T. Z.: Writing – review & editing, conceptualization, funding acquisition, project administration.

Use of AI statement

None.

References

[1] Ralston, J.; Reid, D.; Hargrave, C.; Hainsworth, D. Sensing for advancing mining automation capability: A review of underground automation technology development. *Int. J. Min. Sci. Technol.* **2014**, *24*, 305–310.

[2] Hazrathosseini, A.; Moradi Afrapoli, A. The advent of digital twins in surface mining: Its time has finally arrived. *Resour. Policy* **2023**, *80*, 103155.

[3] Bofill, J.; Abisado, M.; Villaverde, J.; Sampedro, G. A. Exploring digital twin-based fault monitoring: Challenges and opportunities. *Sensors* **2023**, *23*, 7087.

[4] Liu, M. N.; Fang, S. L.; Dong, H. Y.; Xu, C. Z. Review of digital twin about concepts, technologies, and industrial applications. *J. Manuf. Syst.* **2021**, *58*, 346–361.

[5] Adu-Manu, K. S.; Adam, N.; Tapparello, C.; Ayatollahi, H.; Heinzelman, W. Energy-harvesting wireless sensor networks (EH-WSNs): A review. *ACM Trans. Sens. Netw.* **2018**, *14*, 1–50.

[6] Wang, B. C.; Zhou, H. Y.; Li, X. Y.; Yang, G.; Zheng, P.; Song, C.; Yuan, Y. X.; Wuest, T.; Yang, H. Y.; Wang, L. H. Human digital twin in the context of industry 5.0. *Robot. Comput. Integr. Manuf.* **2024**, *85*, 102626.

[7] Belfadel, A.; Hörl, S.; Tapia, R. J.; Politaki, D.; Kureshi, I.; Tavasszy, L.; Puchinger, J. A conceptual digital twin framework for city logistics. *Comput. Environ. Urban Syst.* **2023**, *103*, 101989.

[8] Wang, H.; Chen, X. W.; Jia, F.; Cheng, X. J. Digital twin-supported smart city: Status, challenges and future research directions. *Expert Syst. Appl.* **2023**, *217*, 119531.

[9] Hao, D. N.; Gong, Y. C.; Wu, J. Y.; Shen, Q. H.; Zhang, Z. T.; Zhi, J. Y.; Zou, R.; Kong, W. H.; Kong, L. J. A self-sensing and self-powered wearable system based on multi-source human motion energy harvesting. *Small* **2024**, *20*, 2311036.

[10] Zhou, S. Z.; Li, Z. Y.; Zhou, S. X. A two-degree-of-freedom nonlinear electromagnetic energy harvester in rotational motion. *Mech. Syst. Signal Process.* **2024**, *220*, 111695.

[11] Hao, D. N.; Kong, L. J.; Zhang, Z. T.; Kong, W. H.; Tairab, A. M.; Luo, X.; Ahmed, A.; Yang, Y. W. An electromagnetic energy harvester with a half-wave rectification mechanism for military personnel. *Sustain. Energy Technol. Assess.* **2023**, *57*, 103184.

[12] Nadertehrani, A.; Ziaei-Rad, S.; Eshtehardiha, R. Harvesting vibration energy by quad-stable piezoelectric cantilever beam: Modeling, fabrication and testing. *Eur. J. Mech. A/Solids* **2024**, *107*, 105389.

[13] Sezer, N.; Koç, M. A comprehensive review on the state-of-the-art of piezoelectric energy harvesting. *Nano Energy* **2021**, *80*, 105567.

[14] Lin, Z. W.; Sun, C. C.; Zhang, G. Q.; Fan, E. D.; Zhou, Z. H.; Shen, Z. Y.; Yang, J.; Liu, M. Y.; Xia, Y. S.; Si, S. B. et al. Flexible triboelectric nanogenerator toward ultrahigh-frequency vibration sensing. *Nano Res.* **2022**, *15*, 7484–7491.

[15] Tang, S.; Chang, W. X.; Li, G.; Sun, J. F.; Du, Y.; Hui, X. D.; Tang, Q.; Hu, Z. H.; Li, J. Q.; Chen, J. et al. High performance wide frequency band triboelectric nanogenerator based on multilayer wave superstructure for harvesting vibration energy. *Nano Res.* **2023**, *16*, 6933–6939.

[16] Wang, K. K.; Yao, Y. M.; Liu, Y. X.; Guan, X.; Yu, Y.; Wang, J. L.; Wang, Y. Q.; Li, T. Y.; Cheng, T. H. Self-powered system for real-time wireless monitoring and early warning of UAV motor vibration based on triboelectric nanogenerator. *Nano Energy* **2024**, *129*, 110012.

[17] Tan, D. G.; Zhou, J. X.; Wang, K.; Zhao, X. H.; Wang, Q.; Xu, D. L. Bow-type bistable triboelectric nanogenerator for harvesting energy from low-frequency vibration. *Nano Energy* **2022**, *92*, 106746.

[18] Zhao, Y. C.; Gao, S. H.; Zhang, X.; Huo, W. X.; Xu, H.; Chen, C.; Li, J.; Xu, K. X.; Huang, X. Fully flexible electromagnetic vibration sensors with annular field confinement origami magnetic membranes. *Adv. Funct. Mater.* **2020**, *30*, 2001553.

[19] Chen, X. X.; Guo, H.; Wu, H. X.; Chen, H. T.; Song, Y.; Su, Z. M.; Zhang, H. X. Hybrid generator based on freestanding magnet as all-direction in-plane energy harvester and vibration sensor. *Nano Energy* **2018**, *49*, 51–58.

[20] Koka, A.; Sodano, H. A. High-sensitivity accelerometer composed of ultra-long vertically aligned barium titanate nanowire arrays. *Nat. Commun.* **2013**, *4*, 2682.

[21] Wang, Z. L.; Chen, J.; Lin, L. Progress in triboelectric nanogenerators as a new energy technology and self-powered sensors. *Energy Environ. Sci.* **2015**, *8*, 2250–2282.

[22] Xu, Y. H.; Yang, W. X.; Yu, X.; Li, H. C.; Cheng, T. H.; Lu, X. H.; Wang, Z. L. Real-time monitoring system of automobile driver status and intelligent fatigue warning based on triboelectric nanogenerator. *ACS Nano* **2021**, *15*, 7271–7278.

[23] Fang, Z.; Kong, L. J.; Chen, J. F.; Chen, H. Y.; Zhao, X. Y.; Luo, D. B. Zhang, Z. T. A multi-node self-powered fault detection system by triboelectric-electromagnetic nanosensors for smart transportation. *Nano Energy* **2024**, *128*, 109882.

[24] Fang, Z.; Zhou, Z. J.; Yi, M. Y.; Zhang, Z. T.; Luo, X.; Ahmed, A. A roller-bearing-based triboelectric nanosensor for freight train synergistic maintenance in smart transportation. *Nano Energy* **2023**, *106*, 108089.

[25] Zhang, C. G.; Liu, Y. B.; Zhang, B. F.; Yang, O.; Yuan, W.; He, L. X.; Wei, X. L.; Wang, J.; Wang, Z. L. Harvesting wind energy by a triboelectric nanogenerator for an intelligent high-speed train system. *ACS Energy Lett.* **2021**, *6*, 1490–1499.

[26] Jin, T.; Sun, Z. D.; Li, L.; Zhang, Q.; Zhu, M. L.; Zhang, Z. X.; Yuan, G. J.; Chen, T.; Tian, Y. Z.; Hou, X. Y. et al. Triboelectric nanogenerator sensors for soft robotics aiming at digital twin applications. *Nat. Commun.* **2020**, *11*, 5381.

[27] Zhang, X. Q.; Yu, M.; Ma, Z. R.; Ouyang, H.; Zou, Y.; Zhang, S. L.; Niu, H. K.; Pan, X. X.; Xu, M. Y.; Li, Z. et al. Self-powered distributed water level sensors based on liquid-solid triboelectric nanogenerators for ship draft detecting. *Adv. Funct. Mater.* **2019**, *29*, 1900327.

[28] Zhang, Q. Y.; Barri, K.; Kari, S. R.; Wang, Z. L.; Alavi, A. H. Multifunctional triboelectric nanogenerator-enabled structural elements for next generation civil infrastructure monitoring systems. *Adv. Funct. Mater.* **2021**, *31*, 2105825.

[29] Lee, D.; Kim, D. Dual output from unitary input for a hybrid coaxial triboelectric nanogenerator inspired by a crank engine. *Nano Energy* **2020**, *71*, 104599.

[30] Wang, X. H.; Yin, G. F.; Sun, T.; Xu, X. J.; Rasool, G.; Abbas, K. Mechanical vibration energy harvesting and vibration monitoring based on triboelectric nanogenerators. *Energy Technol.* **2024**, *12*, 2300931.

[31] Wang, C.; Zhang, X. S.; Wu, J.; Yu, X.; Cheng, T. H.; Ma, H. W.; Wang, Z. L. Double-spring-piece structured triboelectric sensor for broadband vibration monitoring and warning. *Mech. Syst. Signal Process.* **2022**, *166*, 108429.

[32] Tang, G.; Cheng, F.; Hu, X.; Huang, B.; Xu, B.; Li, Z. B.; Yan, X. X.; Yuan, D. D.; Wu, W. J.; Shi, Q. F. A two-degree-of-freedom cantilever-based vibration triboelectric nanogenerator for low-frequency and broadband operation. *Electronics* **2019**, *8*, 1526.

[33] Pang, Y. K.; Li, X. H.; Chen, M. X.; Han, C. B.; Zhang, C.; Wang, Z. L. Triboelectric nanogenerators as a self-powered 3D acceleration sensor. *ACS Appl. Mater. Interfaces* **2015**, *7*, 19076–19082.

[34] Jin, L.; Deng, W. L.; Su, Y. C.; Xu, Z.; Meng, H.; Wang, B.; Zhang, H. P.; Zhang, B. B.; Zhang, L.; Xiao, X. B. et al. Self-powered wireless smart sensor based on maglev porous nanogenerator for train monitoring system. *Nano Energy* **2017**, *38*, 185–192.

[35] Shi, Q.; Yang, J. H.; Gui, H.; Gui, Y. G.; Tang, C.; Yu, Y. Q.; Zhao, Z. Y. Self-powered circular-honeycomb triboelectric nanogenerator for vibration energy harvesting and resonance detection of synchronous machine. *Sens. Actuators A Phys.* **2023**, *354*, 114291.

[36] Xiao, X.; Zhang, X. Q.; Wang, S. Y.; Ouyang, H.; Chen, P. F.; Song, L. G.; Yuan, H. C.; Ji, Y. L.; Wang, P. H.; Li, Z. et al. Honeycomb structure inspired triboelectric nanogenerator for highly effective vibration energy harvesting and self-powered engine condition monitoring. *Adv. Energy Mater.* **2019**, *9*, 1902460.

[37] Zhao, H. F.; Shu, M. R.; Ai, Z. H.; Lou, Z. R.; Sou, K. W.; Lu, C. Y.; Jin, Y. C.; Wang, Z. H.; Wang, J. Y.; Wu, C. S. et al. A highly sensitive triboelectric vibration sensor for machinery condition monitoring. *Adv. Energy Mater.* **2022**, *12*, 2201132.

[38] Bhatta, T.; Pradhan, G. B.; Shrestha, K.; Jeong, S. H.; Zhang, S. P.; Kim, H. S.; Park, J. Y. All elastomeric pillars-based triboelectric vibration sensor for self-powered broad range machinery condition monitoring. *Nano Energy* **2023**, *117*, 108929.

[39] Xin, C. F.; Xu, Z. F.; Xie, X.; Guo, H. Y.; Peng, Y.; Li, Z. J.; Liu, L. L.; Xie, S. R. Structure-crack detection and digital twin demonstration based on triboelectric nanogenerator for intelligent maintenance. *Adv. Sci.* **2023**, *10*, 2302443.

[40] Yang, Y. Q.; Shi, Q. F.; Zhang, Z. X.; Shan, X. C.; Salam, B.; Lee, C. Robust triboelectric information-mat enhanced by multi-modality deep learning for smart home. *InfoMat* **2023**, *5*, e12360.

[41] Walter, P. L. Review: Fifty years plus of accelerometer history for shock and vibration (1940-1996). *Shock Vib.* **1999**, *6*, 197–207.

[42] Son, J. D.; Niu, G.; Yang, B. S.; Hwang, D. H.; Kang, D. S. Development of smart sensors system for machine fault diagnosis. *Expert Syst. Appl.* **2009**, *36*, 11981–11991.

[43] Wang, Z. L. Triboelectric nanogenerators as new energy technology for self-powered systems and as active mechanical and chemical sensors. *ACS Nano* **2013**, *7*, 9533–9557.

[44] Chen, J.; Zhu, G.; Yang, W. Q.; Jing, Q. S.; Bai, P.; Yang, Y.; Hou, T. C.; Wang, Z. L. Harmonic-resonator-based triboelectric nanogenerator as a sustainable power source and a self-powered active vibration sensor. *Adv. Mater.* **2013**, *25*, 6094–6099.

[45] Huang, C. M.; Li, Q. T.; Li, J.; Guo, H. Z.; Hao, W. H.; Sheng, K. X.; An, Y. S.; Chen, J. Y.; Zhang, X. Y.; Xu, M. Y. Research on dynamics of bouncing ball in triboelectric nanogenerator. *J. Micromech. Microeng.* **2021**, *31*, 085002.

[46] Luo, A. C. J.; Han, R. P. S. The dynamics of a bouncing ball with a sinusoidally vibrating table revisited. *Nonlinear Dyn.* **1996**, *10*, 1–18.

[47] Li, G. B.; Li, Q. T.; Hao, W. H.; Li, J.; Guo, H. Z.; Zheng, X. Q.; Huang, C. M. Numerical calculation and experimental investigation on optimization of bouncing ball triboelectric nanogenerator. *Nano Energy* **2022**, *104*, 107864.

[48] Niu, S. M.; Liu, Y.; Chen, X. Y.; Wang, S. H.; Zhou, Y. S.; Lin, L.; Xie, Y. N.; Wang, Z. L. Theory of freestanding triboelectric-layer-based nanogenerators. *Nano Energy* **2015**, *12*, 760–774.

[49] Ahmad, M. M.; Khan, N. M.; Khan, F. U. Review of frequency up-conversion vibration energy harvesters using impact and plucking mechanism. *Int. J. Energy Res.* **2021**, *45*, 15609–15645.

[50] Yu, Y.; Li, H. Y.; Zhao, D.; Gao, Q.; Li, X.; Wang, J. L.; Wang, Z. L.; Cheng, T. H. Material's selection rules for high performance triboelectric nanogenerators. *Mater. Today* **2023**, *64*, 61–71.

[51] Lu, C. X.; Han, C. B.; Gu, G. Q.; Chen, J.; Yang, Z. W.; Jiang, T.; He, C.; Wang, Z. L. Temperature effect on performance of triboelectric nanogenerator. *Adv. Eng. Mater.* **2017**, *19*, 1700275.